Water Research 184 (2020) 116157

Contents lists available at ScienceDirect

Water Research

journal homepage: www.elsevier.com/locate/watres

Hierarchical $Bi_2O_2CO_3$ wrapped with modified graphene oxide for adsorption-enhanced photocatalytic inactivation of antibiotic resistant bacteria and resistance genes

Deyi Li [a, 1], Pingfeng Yu [b, c, 1], Xuefei Zhou [a], Jae-Hong Kim [c, d], Yalei Zhang [a, **], Pedro J.J. Alvarez [b, c, *]

[a] State Key Laboratory of Pollution Control and Resource Reuse, Tongji University, Shanghai, 200092, China
[b] Department of Civil and Environmental Engineering, Rice University, Houston, TX, 77005, United States
[c] Nanosystems Engineering Research Center for Nanotechnology Enabled Water Treatment (NEWT), United States
[d] Department of Chemical and Environmental Engineering, Yale University, New Haven, CT, 06520, United States

ARTICLE INFO

Article history:
Received 17 March 2020
Received in revised form
22 June 2020
Accepted 4 July 2020
Available online 6 July 2020

Keywords:
Trap-and-zap
Nitrogen-doped graphene
Surface reactive species
Antibiotic resistance

ABSTRACT

There is growing pressure for wastewater treatment plants to mitigate the discharge of antibiotic resistant bacteria (ARB) and extracellular resistance genes (eARGs), which requires technological innovation. Here, hierarchical $Bi_2O_2CO_3$ microspheres were wrapped with nitrogen-doped, reduced graphene oxide (NRGO) for enhanced inactivation of multidrug-resistant *E. coli* NDM-1 and degradation of the plasmid-encoded ARG (bla_{NDM-1}) in secondary effluent. The NRGO shell enhanced reactive oxygen species (ROS) generation (•OH and H_2O_2) by about three-fold, which was ascribed to broadened light absorption region (red-shifted up to 459 nm) and decreased electron-transfer time (from 55.3 to 19.8 ns). Wrapping enhanced *E. coli* adsorption near photocatalytic sites to minimize ROS scavenging by background constituents, which contributed to the NRGO-wrapped microspheres significantly outperforming commercial TiO_2 photocatalyst. ROS scavenger tests indicated that wrapping also changed the primary inactivation pathway, with photogenerated electron holes and surface-attached hydroxyl radicals becoming the predominant oxidizing species with wrapped microspheres, versus free ROS (e.g., •OH, H_2O_2 and $\bullet O_2^-$) for bare microspheres. Formation of resistance plasmid-composited microsphere complexes, primary due to the π-π stacking and hydrogen bonding between the shell and nucleotides, also minimized ROS scavenging and kept free plasmid concentrations below 10^2 copies/mL. As proof-of-concept, this work offers promising insight into the utilization of NRGO-wrapped microspheres for mitigating antibiotic resistance propagation in the environment.

1. Introduction

The propagation of antibiotic resistant bacteria (ARB) poses a growing threat to public health (Davies and Davies, 2010; O'Neill, 2016), underscoring the need to consider the occurrence and fate of ARB in water infrastructure. Some wastewater treatment plants (WWTPs) may serve as breeding grounds and point sources for ARB and extracellular antibiotic resistance genes (eARGs) that contribute to the environmental resistome (Ju et al., 2016; Luo et al., 2014). Furthermore, conventional secondary effluent disinfection approaches (e.g., chlorination and ultraviolet (UV) radiation) exhibit relatively low efficiency to mitigate the discharge of ARB and eARGs (He et al., 2019; Lorenz and Wackernagel, 1994; Luo et al., 2011), and residual disinfectants may enhance ARG horizontal transfer, contributing to resistance propagation (Dotson et al., 2010; Li et al., 2016; Zhang et al., 2017). Thus, there is a critical need for technological innovation to develop robust and sustainable approaches to mitigate antibiotic resistance dissemination through efficient ARB inactivation and associated eARGs degradation.

* Corresponding author. Department of Civil and Environmental Engineering, Rice University, Houston, TX, 77005, United States.
** Corresponding author.
E-mail addresses: zhangyalei@tongji.edu.cn (Y. Zhang), alvarez@rice.edu (P.J.J. Alvarez).
[1] Joint first authors: D. Li and P. Yu contributed equally and were ordered alphabetically.

https://doi.org/10.1016/j.watres.2020.116157
0043-1354/

Photocatalysis has received significant attention as a potential eco-friendly disinfection process for eliminating waterborne microbial contaminants, including ARB (Giannakis et al., 2018; Pelaez et al., 2012; Zhao et al., 2014a). The process involves production of reactive oxygen species (ROS) such as hydroxyl radicals (•OH) and superoxide ($O_2^{\bullet-}$), as well as electron holes (h^+), upon UV irradiation (Table S1). These oxidizing species can efficiently inactivate bacteria by attacking essential biomolecules (e.g., lipids, proteins, and DNA) (Cho et al., 2004; Ren et al., 2018; Xia et al., 2015). Three-dimensional (3D) hierarchical microspheres composed of 2D photoactive nanosheets exhibit high specific surface area to facilitate light harvesting and photocatalytic performance (Liang et al., 2017; Zhang et al., 2013), while their relatively large size enables cost-effective separation and recovery (Zhang et al., 2018). We previously showed that nanosheet-assembled $Bi_2O_2CO_3$ microspheres can be easily composited with electron-shuttling reduced graphene oxide (RGO) to promote electron transfer and increase ROS production (Zhang et al., 2014). However, while enhanced ROS generation may improve disinfection (Moreira et al., 2018), a higher rate of cells lysis increases the release of eARGs. Due to ROS dilution and scavenging by background constituents (e.g., carbonates, soluble microbial products (SMPs), and natural organic matter), eARGs released in bulk water away from photocatalytic sites may escape treatment (Dunlop et al., 2015; Ribeiro et al., 2019). Accordingly, previous work showed that RGO-enhanced photocatalytic disinfection of ARB did not efficiently degrade the associated eARGs in wastewater (Karaolia et al., 2018). Thus, it is important to enhance bacterial and eARG adsorption near photocatalytic sites for more efficient ROS utilization (i.e., trap-and-zap strategy) (Zhang et al., 2018).

We postulate that nitrogen doping of the RGO shell can improve bacterial adhesion to microspheres due to a less negative zeta potential than undoped RGO (Hasan et al., 2012; Smith et al., 2019), which decreases electrostatic repulsion and thus increase the probability of catalyst-bacteria collision (Xue et al., 2018; Zhao et al., 2014b). Subsequently, bacteria can be adsorbed by the catalyst due to hydrophobic interaction between hydrophobic amino acids on bacterial surfaces and the photocatalyst surface (e.g., graphitic basal planes). Bacterial adsorption near photocatalytic sites is not only conducive to more efficient disinfection, but also may enhance the immediate capture and degradation of eARGs that are released due to bacterial cell lysis. Furthermore, nitrogen doping may accelerate electron transfer and enhance ROS generation by decreasing defects within the NRGO plane, and improving the interfacial contact between NRGO and the photocatalyst (Mou et al., 2014; Xu et al., 2016).

Here, we report the synthesis of novel NRGO-wrapped $Bi_2O_2CO_3$ microspheres (NGWM), and demonstrate their efficacy for simultaneous photocatalytic ARB inactivation and eARGs degradation in a secondary effluent polishing context. Enhanced bacterial adsorption and inactivation, as well as eARG degradation, were confirmed by direct comparisons versus treatment with bare $Bi_2O_2CO_3$ microspheres or undoped RGO-wrapped $Bi_2O_2CO_3$ microspheres (GWM). The photocatalytic mechanism was investigated through ROS scavenging tests, and oxidative stress to the ARB was assessed by quantifying cell membrane integrity and antioxidant enzymatic activity. We discerned the interfacial mechanisms for enhanced eARGs adsorption and degradation relative to uncoated catalyst. Benchmarking experiments were also performed using a commercial TiO_2 photocatalyst to demonstrate the applicability of NGWM for municipal wastewater treatment effluent disinfection and associated mitigation of antibiotic resistance propagation.

2. Materials and methods

2.1. Chemicals, reagents and bacterial strains

Bismuth citrate (≥99%), urea (≥97%), ethanol (≥99.5%), (3-aminopropyl)trimethoxysilane (APTMS, ≥97%), *p*-chlorobenzoic acid (pCBA, ≥[X]%), hydrazine monohydrate (N_2H_4, ≥98%), potassium iodide (KI, ≥99%), isopropanol (IPA, ≥99%), superoxide dismutase (SOD), sodium pyruvate (SP, ≥99%), protein carbonyl content assay kit, and 2,7-dichlorodihydrofluorescein diacetate (DCFH-DA, ≥97%) were purchased from Sigma-Aldrich and used as received. Single layer graphene oxide power (GO, ≥99%) was purchased from Nanjing XFNANO MaterialsTech Co., Ltd. Commercial TiO_2 powder (Evonik, P25) was purchased from Sigma-Aldrich (Fig. S1).

The bacterial strain used in this study was *E. coli* NDM-1 (ATCC BAA-2452) carrying a pET-29a (+) plasmid-encoded bla_{NDM-1} gene. Multidrug-resistant *E. coli* NDM-1 was used as a representative ARB, and the plasmid-encoded β-lactam resistant bla_{NDM-1} gene (coding for New Delhi metallo-beta-lactamase) was the target ARG. The bacteria were incubated in LB broth medium with 100 mg/L ampicillin at 37 °C for overnight with shaking at 120 rpm and then washed with phosphate buffer solution (PBS, pH 7.0) three times before photocatalytic reactions. Total viable bacteria were counted by a plate assay method using Difco standard bacterial count agar (BD, Sparks, MD) and expressed as colony-forming-units (CFU).

2.2. Photocatalyst synthesis and characterization

Hierarchical $Bi_2O_2CO_3$ microspheres were synthesized by a hydrothermal method as previously described (Zhang et al., 2014). The microspheres were amine-functionalized by APTMS and then wrapped by graphene oxide (GO) sheet through the electrostatic interactions and dehydration condensation reaction. Subsequently, the corresponding amount of N_2H_4 was added into the GO wrapped $Bi_2O_2CO_3$ microspheres with vigorous stirring for 30 min. The mixed suspension was then transferred into a Teflon stainless steel autoclave and autoclaved at 80 °C for 3 h to achieve GO reduction and N doping simultaneously. Specifically, microspheres should be wrapped by GO before N doping to reduce the electrostatic repulsion between the amine-functionalized $Bi_2O_2CO_3$ microspheres and GO shell. After the hydrothermal reaction, the final mixture was washed with DI water and dried at 60 °C for 24 h under vacuum to obtain NGWM microspheres.

The morphology of the catalysts was characterized by a scanning electron microscopy (SEM, Quanta 200 FEG, FEI) and a high-resolution transmission electron microscopy (HR-TEM, Hitachi S-3000N). The crystal structures were characterized by an X-ray diffraction (XRD, D/max2550VB3+/PC, Rigaku). Chemical functional groups were determined by X-ray photoelectron spectroscopy (XPS, Perkin Elmer PHI 5000 ESCA System) and Fourier transform infrared spectrometry (FTIR, Nicolet 5700, Thermofisher, USA). Light absorption was characterized by a UV−visible diffuse reflectance spectroscopy (UV−vis DRS, BWS002, BWtek).

2.3. Photocatalytic bacterial inactivation and model fitting

Reactions were conducted in 150-mL quartz photocatalytic reactors in a black acrylic box. UVA-visible light was provided by a 300W xenon lamp (PerfectLight PLS-SXE300C, USA) with a band-pass filter ($340 < \lambda < 700$ nm). The incident radiation power of UVA-visible light was measured by a radiometer (PM100D/S425C, Thorlabs, America) and UVA-visible incident light intensity was 8.68×10^{-6} E/L·s (Zhou et al., 2015). The reaction temperature was kept at 25 ± 1 °C by continuous water circulation around the

reactor. Inactivation tests were conducted in PBS and 0.22-μm membrane-filtered WWTP effluents with photocatalyst (200 mg/L) and a representative bacteria (10^8 CFU/mL) (Zhang et al., 2010b). The secondary effluent used in this work (Table S2) came from Quyang Wastewater Treatment Plant in Shanghai. The adsorption-desorption equilibrium of bacteria on the photocatalysts was achieved by magnetically stirring for 60 min under dark. Samples were collected at regular interval, and the viable bacterial density was measured by the plate assay method (Ma et al., 2016). Bacterial abundance and dead/live ratio were measured with a fluorescence microscope (Olympus IX71, Japan) after staining with SYTO 9 and propidium iodide (PI) using a Live/DEAD BacLight kit (Invitrogen AG, Basel, Switzerland) (Li et al., 2017).

Photocatalytic inactivation data were analyzed using the following "log-linear with shoulder and tail" model (Geeraerd et al., 2005; Spasiano et al., 2015):

$$N(t) = (N_0 - N_{res}) \times e^{-kt} \times \frac{e^{kS}}{1 + (e^{kS} - 1) \times e^{-kt}} + N_{res} \quad (1)$$

where N_{res} (log CFU) is the live bacterial concentrations after t-min inactivation, S (min) represents the shoulder length of the lag phase, and k (min^{-1}) is the disinfection rate constant of the "log-linear" period (Ng et al., 2016). These parameters were obtained using the Geeraerd and Van Impe Inactivation Model Fitting Tool (GInaFit, version 1.7) through curve fitting.

2.4. ROS generation efficiency and scavenger experiments

Photocatalysis can produce reactive species (•OH, H_2O_2, $•O_2^-$ and h^+) that are potentially involved in the inactivation of bacterial cells and water disinfection. ROS generation efficiency (i.e., •OH, H_2O_2) was analyzed to evaluate the photoactivity of different photocatalysts. Briefly, *p*CBA was chosen as a probe to detect the steady-state concentrations of •OH (Cho et al., 2004). H_2O_2 production was determined by the N,N-diethyl-p-phenylenediamine (DPD) photometric method (Bader et al., 1988). ROS scavenger experiments were conducted to distinguish the contributions of different ROS generated by NGWM. The scavengers used in this study were SP for H_2O_2, IPA for •OH, SOD for $•O_2^-$ and potassium iodide (KI) for surface-bound species (i.e., h^+ and $•OH_{ads}$) (Giandomenico et al., 1997; Xia et al., 2013; Zhang et al., 2018). We recognize that there may be potential differences in the affinity of different ROS scavengers to catalyst surfaces before and after coating, which may confound interpretation of which ROS played significant roles. Thus, ROS scavengers were added in excess to ensure that their potential depletion due to sorption did not limit their ability to scavenge photogenerated ROS.

2.5. Bacterial response to ROS and cellular damage assessment

Systematic experiments were conducted to investigate the bacterial responses to and damages caused by ROS. Briefly, the cell membrane integrity was examined by the K^+ leakage assay, protein leakage assay, and ATP synthesis ability (Wang et al., 2012; Xia et al., 2016). The activities of CAT and SOD were measured to indicate the intracellular enzymatic antioxidant activity (Sun et al., 2014). The total protein oxidation level was quantified to assess the extent of protein oxidative damage (Xia et al., 2015). Cell mineralization was calculated by the difference of total organic carbon (TOC) levels before and after treatment using a total organic carbon analyzer (TOC-V CPN, Shimadzu, Japan). Additionally, the intracellular ROS (iROS) levels were measured using the fluorescent probe 2,7-dichlorodihydrofluorescein diacetate (DCFH-DA) method. Briefly, 5 mL bacterial suspension sample was collected and 5 μL DCFH-DA solution (5 mM) was added. Then, the mixture was vortexed and incubated at 37 °C for 30 min under dark. Subsequently, the mixed suspension was concentrated with tubular ultrafiltration modules (Amicon Ultra-4, 10K, Millipore) to 200 μL for the fluorescence detect at 525 nm with 488 nm excitation wavelength using a Tecan M1000 fluorescence reader (Tecan, Männedorf, Switzerland) (Xia et al., 2016).

2.6. DNA biomarker quantification

To quantify the release and degradation of ARG during photocatalytic inactivation, intracellular ARGs (iARGs) and eARGs were harvested separately and then quantified by quantitative polymerase chain reaction (qPCR) (Jiang et al., 2017). Specifically, bacterial suspensions at various intervals were sampled and then centrifuged to harvest the cells. The intracellular DNA were extracted from the cell pellet using a UltraClean DNA Isolation Kit (MoBiO Laboratories, USA) following the manufacturer's instructions. The extracellular DNA was collected and concentrated via the DNA purification column (Sangon, China) after lysozyme, RNase A, and proteinase K treatment (Jiang et al., 2017). The details of qPCR procedures and primer sets, standard curve generation, and the DNA recovery efficiency calculation are available in the supporting information.

2.7. Catalyst-plasmid interaction analysis

Plasmid pET-29a (+) (bla_{NDM-1} encoded) was selected as the model plasmid and mixed well with catalysts in DI water at 25 °C for 30 min. The bound plasmid was stained with SYBR® Green I (Thermofisher, USA) and observed using a fluorescence microscopy (Nikon Eclipse 80i, Japan) following the method by (Rinta-Kanto et al., 2004). The interfacial interaction of the photocatalyst and plasmid DNA was analyzed by a confocal Raman microscopy/spectrometer system (Invia Reflex, Renishaw, UK) and an FTIR with attenuated total reflection (ART) module (Nicolet 5700, Thermofisher, USA). Additionally, the plasmid concentration was measured by qPCR, and the plasmid binding capacity was calculated based on the following equation: binding capacity = $(C_0 - C_t)/C_w$, where C_0 = original plasmid concentration, C_t = residual plasmid concentration, and C_w = catalysts concentration) (Yu et al., 2016).

2.8. Catalyst stability tests

The stability of NGWM photoactivity was investigated over ten cycles of repetitive use in wastewater effluent. The catalysts were collected by a microfiltration (3-μm membrane filter, Millipore-Sigma) and dried for the next cycle after each photocatalytic inactivation experiment. The catalysts after the tenth cycles were characterized with XPS to discern possible chemical changes on NGWM. To assess the extent of photocorrosion, Bi ions (Bi^{3+}) concentration in the filtrate was monitored through an inductively coupled plasma (ICP, Agilent 720 ES, Japan) after ten cycles to estimate the mass loss of NGWM.

2.9. Statistical analysis

All tests were run in triplicate (n = 3) and data were expressed as means ± SD. Student's T-test (unpaired, two-tailed) was used to determine the significance of the differences between treatments at the 95% level ($p < 0.05$).

3. Results and discussion

3.1. $Bi_2O_2CO_3$ microspheres were successfully wrapped with NRGO nanosheets

NGWM microspheres (1.5 ± 0.5 μm in diameter) exhibited a core-shell structure with a rose-like core of $Bi_2O_2CO_3$ nanosheets, which was completely wrapped by a thin layer of NRGO (Fig. 1A–C). XPS spectra confirm the chemical bonds that constitute $Bi_2O_2CO_3$ and NRGO composite materials (Fig. 1D–F & Figs. S2A–B). Specifically, the C-Bi bond observed at 164.2 eV (Bi 4f spectrum) and 281.2 eV (C 1s spectrum) suggests formation of chemical bond at the interface of $Bi_2O_2CO_3$ core and NRGO shell (Fig. 1D & Fig. S2A). The C 1s spectrum of NGWM (Fig. 1D) also shows the presence of C-C, C-N, and C-O from NRGO at 284.8, 285.8, and 286.7 eV, respectively (Zhang et al., 2014). Specifically, the C-C peak from C 1s spectrum of $Bi_2O_2CO_3$ (Fig. S2B) at 284.8 eV refers to the adventitious carbon added for binding energy correction. Nitrogen doping was verified by the peaks at 398.1, 399.6, and 401.6 eV (Fig. 1E), which correspond to pyridine-N, pyrrole-N, and graphite N from NRGO, respectively (Xu et al., 2016). As expected, the oxygen-containing functional groups from NRGO (i.e., -OH, -CO(OH), and C=O detected at 533.18, 532.18, and 531.22 eV, respectively) and the Bi-O bond from $Bi_2O_2CO_3$ (529.58 eV) were identified from the O 1s spectrum of NGWM (Fig. 1F). Surface wrapping did not affect the crystallites of the hierarchical core, as $Bi_2O_2CO_3$ microspheres, GWM, and NGWM all showed identical diffraction peaks of tetragonal phase $Bi_2O_2CO_3$ (Fig. S2C) (Dong et al., 2011).

3.2. Wrapping the photocatalyst with NRGO enhanced ROS generation and facilitated bacterial adsorption, improving disinfection

Nitrogen doping (i.e., NGWM) significantly facilitated ROS generation (Fig. 2A) through accelerated electron transfer and enhanced visible light absorption intensity (Figs. S2D and S3). The average photon emission lifetime (from electron/hole pair recombination) of NGWM (τ = 15.4 ns) was much shorter than that of $Bi_2O_2CO_3$ microspheres (τ = 69.0 ns) and GWM (τ = 30.7 ns) (Table 1 & Fig. S3), which is likely due to the ultrafast electron transfer process from $Bi_2O_2CO_3$ to NRGO. Additionally, nitrogen doping decreased the defects on the graphene sheets, as measured by Raman spectroscopy. The intensity ratio of the D and G bands (I_D/I_G) represents the relative concentration of sp^3 hybridized defects compared to the sp^2 hybridized carbon network (Liang et al., 2011). Specifically, I_D/I_G value of NGWM decreased by 6.5% compared to GWM (Fig. S4), which corroborates that nitrogen-doping decreased the abundance of defects on NRGO. Additionally, N atoms could also serve as active sites for electron transfer or redox reactions (Xu et al., 2016). Decreasing defects within the NRGO plane and improving the interfacial contact between NRGO and the photocatalyst resulted in a higher electron-transfer efficiency (η = 77.78%) for NGWM compared to GWM (η = 55.51%) (Mou et al., 2014). Due to NRGO wrapping, NGWM exhibited an red-shifted absorption edge up to 459 nm attributed to the formation of Bi-C bond with an enhanced broadband absorption ranging from 460 to 800 nm due to the presence of graphene (Figs. S2A and D) (Zhang et al., 2010a, 2014). Consistently, increased ROS generation

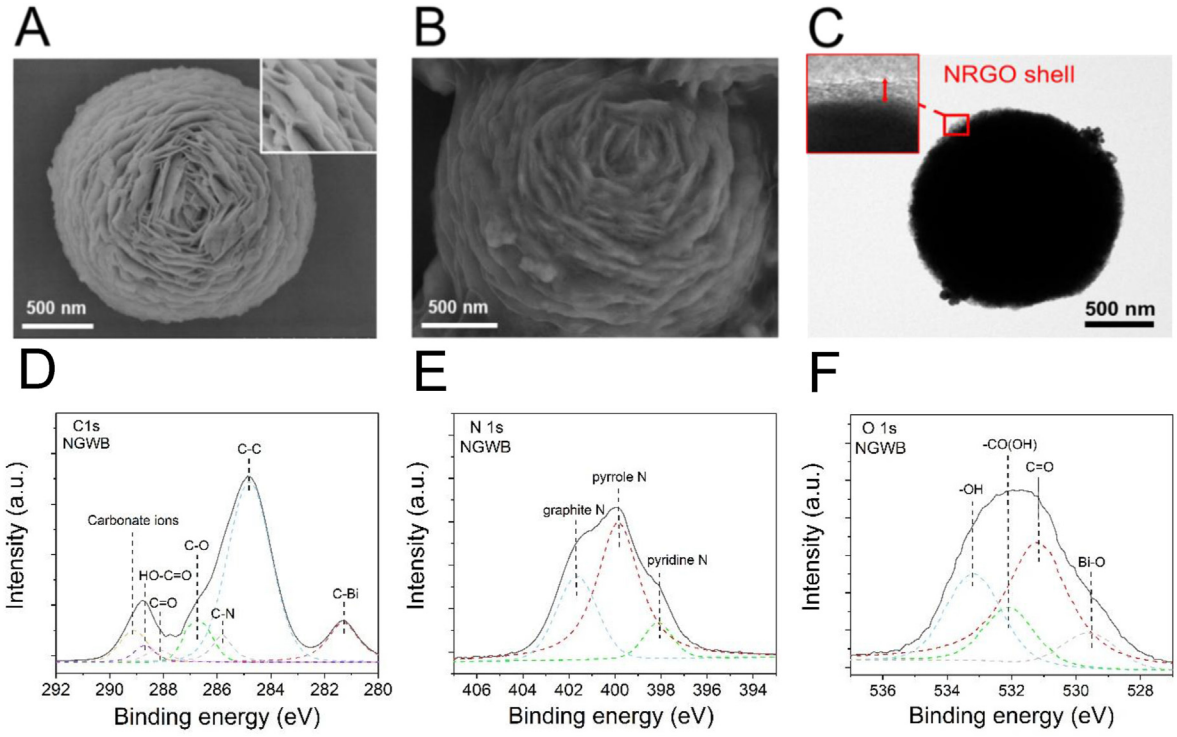

Fig. 1. Characterization of 3D hierarchical $Bi_2O_2CO_3$ microspheres wrapped with NRGO shell. (A) SEM image of the 3D hierarchical $Bi_2O_2CO_3$ composed of many layers of 2D nanoplates around 15 nm thick (insertion). (B) SEM image of NGWM core-shell structure with relatively wrinkled surface. (C) HR-TEM image of NRGO shell (10–15 nm, red arrow). (D-E) XPS spectra of NGWM depicting $Bi_2O_2CO_3$ microspheres wrapped with NRGO shell. The peaks at 281.2 and 285.8 eV are ascribed to the C-Bi and C-N bonds, respectively. The peaks at 398.1, 399.6, and 401.6 are ascribed to the pyridine N, pyrrole N, and graphite N, respectively. (For interpretation of the references to colour in this figure legend, the reader is referred to the Web version of this article.)

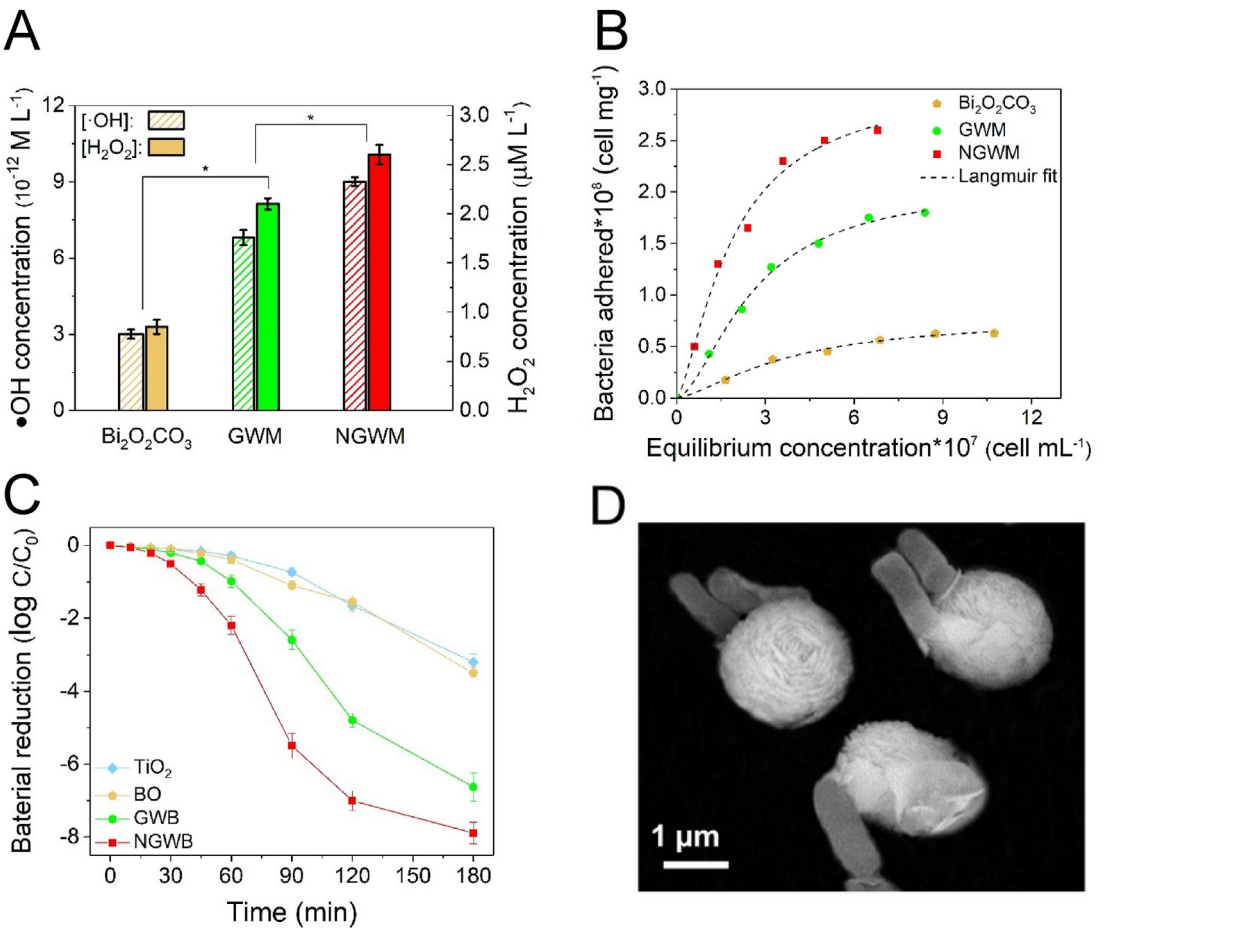

Fig. 2. Influence of NRGO wrapping on *E. coli* NDM-1 adsorption and photocatalytic inactivation. (A) NRGO wrapping significantly enhances ROS generation, which was ascribed to accelerated electron transfer and broadened light absorption region (Fig. S2D&S3). Asterisks (*) represent significant differences ($p < 0.05$) between treatments, based on Student's t-test. (B) Adsorption isotherms for *E. coli* NDM-1 with various photocatalysts in secondary effluent. (C) Photocatalytic *E. coli* inactivation by UVA-visible light irradiation ($340 < \lambda < 700$ nm, 8.68×10^{-6} E/L·s) in secondary effluent. (D) SEM image of *E. coli* adsorbed onto photocatalyst in secondary effluent. Error bars represent ± one standard deviation from the mean of triplicate measurements.

Table 1
Kinetic Analysis of Time-Resolved Emission Decay with various photocatalysts.

	Average emission lifetime[a] (τ, ns)	Electron-transfer lifetime (τ_{CT}, ns)	Electron-transfer efficiency (η, %)	$A_1/(A_1+A_2)$	τ_1 (ns)	$A_2/(A_1+A_2)$	τ_2 (ns)
$Bi_2O_2CO_3$	69.0	–	–	53.0	6.4	46.9	75.0
GWM	30.7	55.3	55.5	67.7	2.3	32.3	33.6
NGWM	15.4	19.8	77.8	88.5	0.7	11.5	19.3

a. The average emission lifetime of TRPL (τ): $\tau = (A_1\tau_1^2+A_2\tau_2^2)/(A_1\tau_1+A_2\tau_2)$, where τ_1 and τ_2 refer to fast and slow component of TRPL spectrum, respectively.
b. Electron-transfer lifetime (τ_{CT}): $\tau_{CT} = (\tau_{Bi}\tau_C)/(\tau_{Bi}-\tau_C)$, where τ_{Bi} refers to the average lifetime of $Bi_2O_2CO_3$ and τ_C refers to the average lifetime of NGWM and GWM, respectively.
c. Electron-transfer efficiency (η): $\eta = \tau_C/\tau_{CT}$.

(i.e., •OH and H_2O_2) was observed with NGWM under UVA-vis irradiation, relative to GWM and bare microspheres (Fig. 2A & Fig. S5).

To investigate the effect of NRGO on bacterial adhesion, equilibrium adhesion isotherms for *E. coli* NDM-1 were determined with various photocatalysts. NGWM showed a significant improvement in adsorption capacity for bacteria in secondary effluent ($3.08 \pm 0.27\times10^8$ CFU/mg catalyst) compared to $Bi_2O_2CO_3$ microspheres ($0.78 \pm 0.09\times10^8$ CFU/mg catalyst) and GWM ($2.07 \pm 0.18\times10^8$ CFU/mg catalyst) (Fig. 2B & Table S3). Apparently, nitrogen doping increased the zeta potential of NGWM due to protonation of the lone-pair electron on doped-nitrogen (Table S4), decreasing electrostatic repulsion of negatively-charged bacteria (Smith et al., 2019). The flexibility (Koenig et al., 2011) and corrugation (Meyer et al., 2007) of RGO and NRGO surfaces would also enhance bacterial membrane adhesion compared with bare $Bi_2O_2CO_3$ microspheres (Hu and Zhou, 2013). Additionally, NRGO and RGO wrapping improved bacterial affinity for the microspheres through enhanced hydrophobic interaction between bacterial surface proteins and the photocatalyst surface (e.g., hydrophobic amino acids in pilin proteins interacting with graphitic basal planes) (Vesper, 1987; Xue et al., 2018). Despite some background organics could also be adsorbed to the catalysts through hydrophobic interactions, the decreased electrostatic repulsion as well as the flexibility and corrugation properties of NRGO surface facilitated bacterial adsorption to NRGO relative to GWM and $Bi_2O_2CO_3$

microspheres (Fig. S6).

Due to the synergetic effect of enhanced ROS generation and increased bacterial adsorption, NGWM exhibited the highest disinfection rate constant ($k = 0.302 \pm 0.025$ CFU $ml^{-1}min^{-1}$ in PBS and $k = 0.193 \pm 0.017$ CFU $ml^{-1}min^{-1}$ in secondary effluent) (Fig. S7 & Table S5). Also, approximately 6-log inactivation of NDM-1 was achieved within 90 min in PBS and 120 min in secondary effluents under UVA-visible irradiation (8.68×10^{-6} E/L·s). The photocatalytic disinfection rate constant of NGWM in secondary effluents was 3.2, 3.1, and 1.6 times faster than that of TiO_2, $Bi_2O_2CO_3$, and GWM, respectively. Control experiments confirmed that the bactericidal effect of photocatalysts alone (in the dark) and Xenon lamp irradiation alone without photocatalysts were negligible (Fig. S8).

3.3. Bacterial adsorption to NGWM enhanced the contribution of surface-bound photogenerated species in photocatalytic disinfection

The inactivation of *E. coli* NDM-1 in the presence of various scavengers was investigated to gain further insight into the photocatalytic mechanism. ROS scavengers were added in excess to ensure that their potential depletion due to sorption did not limit their ability to scavenge photogenerated ROS (Fig. S9). Wrapping the catalyst with NRGO increased bacterial affinity (Fig. 2C) and resulted in *E. coli* inactivation primarily through a surface bound reactive species (e.g., h^+ and $\bullet OH_{ads}$). This was evidenced by dramatic inhibition of photoactivity by 75.5% in the NGWM photocatalytic system (Fig. 3A & Fig. S10) in the presence of KI (h^+ and $\bullet OH_{ads}$ scavenger). In contrast, the photoactivity for bare $Bi_2O_2CO_3$ microspheres was significantly inhibited by isopropanol ($\bullet OH$ scavenger, 55.6% inhibition), sodium pyruvate (H_2O_2 scavenger, 61.8% inhibition) and superoxide dismutase ($\bullet O_2^-$ scavenger, 50.8% inhibition) (Fig. 3B & Fig. S10). This inhibition of dissolved ROS was much larger than that observed for NGWM (Fig. 3A), demonstrating that free ROS (e.g., $\bullet OH$, H_2O_2 and $\bullet O_2^-$) are more important for *E. coli* inactivation with bare $Bi_2O_2CO_3$ microspheres.

Photogenerated h^+ and $\bullet OH_{ads}$ can directly inactivate adsorbed bacteria by interrupting the electron transport respiratory chain (via electron shuttling between bacteria and h^+) or generate ROS (e.g., $\bullet OH$, H_2O_2 and $\bullet O_2^-$) to attack bacteria (Teng et al., 2019; Zhao et al., 2018). In contrast, due to insufficient bacterial affinity, the bare $Bi_2O_2CO_3$ microsphere surface does not favor direct contact with ARB, and the inactivation process is primarily mediated by the free ROS (e.g., $\bullet OH$, H_2O_2 and $\bullet O_2^-$) that diffuse away from photocatalyst surface sites. The combination of more direct contact (i.e., increased bacterial adsorption) and surface reactive species shows improved ARB disinfection for NGWM compared to GWM and bare $Bi_2O_2CO_3$ microspheres.

3.4. NRGO wrapping enhanced the disruption of bacterial defense systems

As expected, more cell membrane damage was caused by NGWM compared to GWM and $Bi_2O_2CO_3$ microspheres during treatment (Fig. 4A and B). As the reactions progressed, PI-stained cells became more dominant (Fig. S11), and K^+ increasingly leaked out of the cytoplasm (Fig. 4A), indicating more severe cell membrane damage by the increased level of extracellular ROS. Furthermore, bacterial ATP levels dramatically decreased with photocatalytic treatment (Fig. 4B), suggesting that ATPase associated with the cell membrane was also damaged by the extracellular ROS. It has been reported that H_2O_2 can penetrate through the cell membrane and react with Fe^{2+} in the cytoplasm to generate intracellular $\bullet OH$ (intracellular Fenton reaction) (Gogniat and Dukan, 2007). The accelerated destruction of the cell membrane apparently allowed more extracellular ROS (e.g., H_2O_2) to enter the cytoplasm, which further promoted the collapse of bacterial antioxidative enzymes (Fig. 4C & 4D). NGWM resulted in more iROS accumulated in the first 30 min, relative to GWM and $Bi_2O_2CO_3$ microspheres. The iROS concentration exhibited a bell-shaped pattern as a function of reaction time in all the reactions (Fig. 4D). The decrease in iROS after the peak concentration might be due to iROS dispersion into the bulk solution as bacteria lysed. Overall, enhanced extracellular and intracellular ROS generation through NRGO wrapping accelerated the destruction of bacterial defense systems and promoted severe oxidative damage to other functional biomolecules (Figs. S12 and S13).

3.5. NGWM-plasmid binding enhanced photocatalytic degradation of the plasmid-encoded bla_{NDM-1} gene

As with ARB inactivation, NGWM demonstrated enhanced ARG

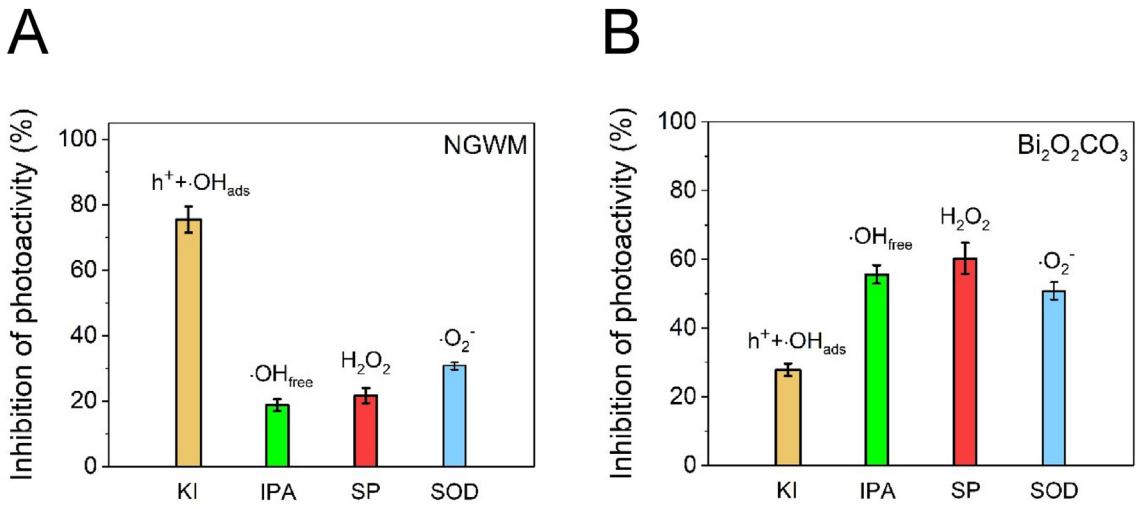

Fig. 3. Importance of different reactive species during photocatalytic inactivation of *E. coli* NDM-1. The microspheres were irradiated by UVA-visible light ($340 < \lambda < 700$ nm, 8.68×10^{-6} E/L·s). The scavengers utilized were 1 mM of isopropanol (IPA) for hydroxyl radicals, 100 kU/L of superoxide dismutase (SOD) for $\bullet O_2^-$, 10 mM of potassium iodide (KI) for electron holes and 10 mM sodium pyruvate (SP) for H_2O_2 for H_2O_2. Error bars represent ± one standard deviation from the mean of triplicate measurements. Photoactivity inhibition was calculated as follows: $(1 - k_{scavenger}/k_{control}) \times 100\%)$.

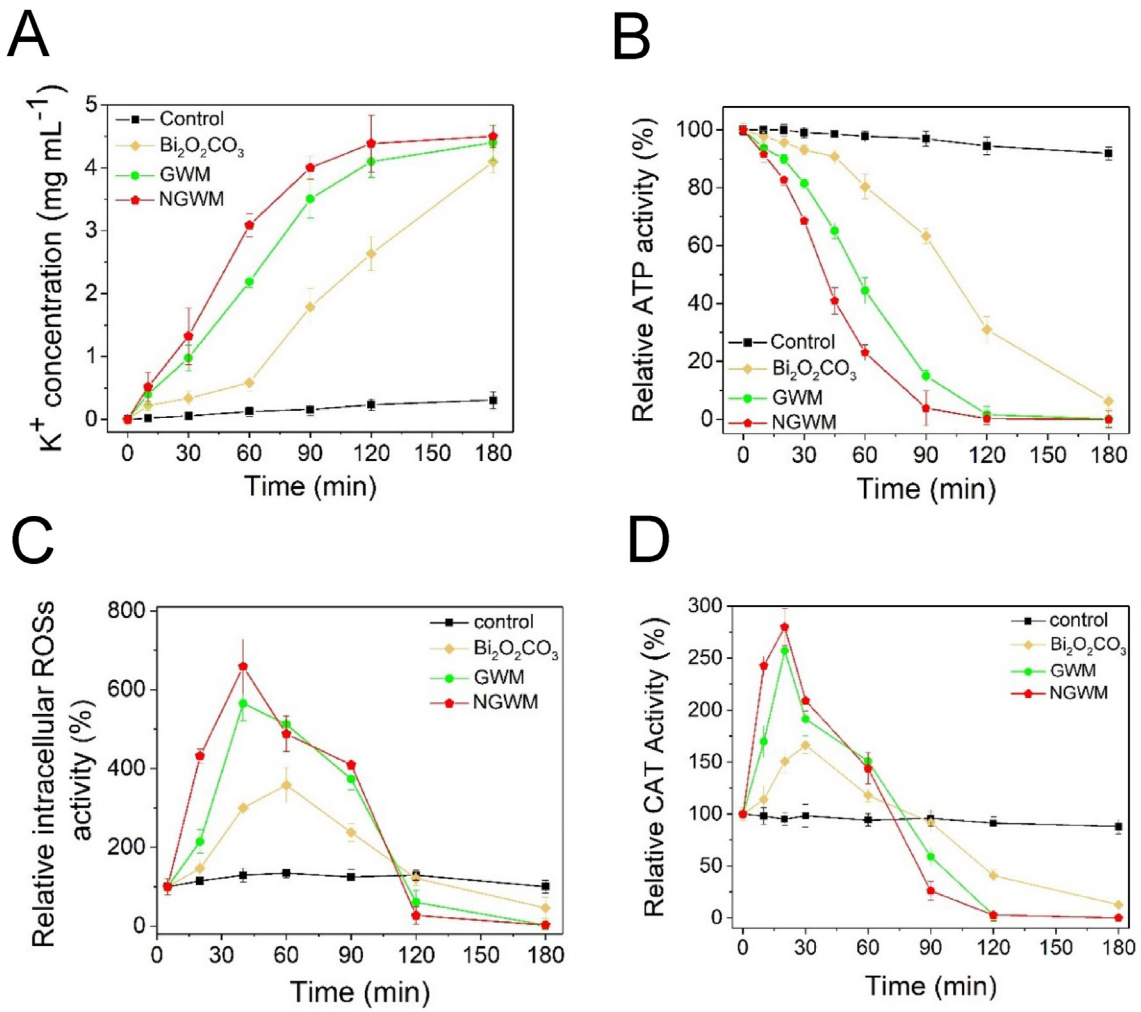

Fig. 4. Cell membrane damage and intracellular antioxidant enzyme inactivation during photocatalytic treatment ($340 < \lambda < 700$ nm, 8.68×10^{-6} E/L·s). NGWM released more potassium ions (K^+) from the cytoplasm (A) and decreased intracellular ATP generation more significantly (B) than $Bi_2O_2CO_3$. Intracellular antioxidant enzyme (i.e., CAT) was induced faster in NGWM (C) and intracellular ROS activity (D) was higher relative to $Bi_2O_2CO_3$. The control experiments were UVA-visible light ($340 < \lambda < 700$ nm, 8.68×10^{-6} E/L·s) alone without any photocatalysts. Error bars represent ± one standard deviation from the mean of triplicate measurements.

(both eARGs and iARGs) degradation, relative to GWM and $Bi_2O_2CO_3$ microspheres. Under UVA-visible light irradiation ($340 < \lambda < 700$ nm, 8.68×10^{-6} E/L·s), NGWM reduced the level of i-bla_{NDM-1} genes by approximately 5.0 log within 120 min and the remaining eARGs was less than the detection limit (2-log copies mL^{-1}) (Fig. 5). Control experiments confirmed the lack of ARG degradation with UVA-visible light irradiation alone (Fig. S8). NGWM began degrading i-bla_{NDM-1} genes significantly earlier than GWM and $Bi_2O_2CO_3$ microspheres. This was likely due to the accelerated destruction of bacterial defense systems (e.g., cell membrane and antioxidative enzymes) mediated by NGWM, which was not as rapid in the other catalyst systems. Subsequently, the abundance of both e-bla_{NDM-1} and i-bla_{NDM-1} genes decreased as treatment time increased (Fig. 5). Note that enhanced ARB adsorption was achieved by NGWM (Fig. 2B), which might shorten the diffusion distance of eARGs from the decayed ARB to the microsphere's surface and photocatalytic sites (e.g., h^+). This would facilitate immediate capture and degradation of the released eARGs, and thus possibly mitigate ROS dilution and scavenging by background constituents. Accordingly, photocatalytic treatment with NGWM outperformed other treatments: less than 2-log eARGs (copies mL^{-1}) were detected within 120 min with NGWM, versus 7.5-log with TiO_2, 7.4-log with $Bi_2O_2CO_3$ microspheres, and 4.5-log with GWM (Fig. 5B). Remarkably, the increase in eARGs abundance (due to release from dead cells) was efficiently mitigated by NGWM compared to other photocatalysts (Fig. 5), corroborating that plasmid DNA released from impaired cells could be effectively adsorbed (with increasing ARB adsorption and plasmid-DNA binding capacity) for more efficient oxidation (Fig. 2B & Fig. S14). Background constituents in the effluent (including naturally occurring ROS scavengers) hindered photocatalytic degradation of eARGs by both TiO_2 and NGWM relative to treatment in PBS solution (Fig. S15). Nevertheless, NGWM enhanced bacterial and plasmid DNA adsorption near photocatalytic sites, and was thus less susceptible to such inhibitory effects than TiO_2.

Plasmids were introduced to verify the interaction between ARG and the NGWM surface during adsorption and photocatalysis. Green fluorescent microspheres (Fig. S16) were observed after mixing NGWM with SYBR-stained plasmids but not before mixing, which indicated that plasmids were adsorbed onto the NGWM surface. The Raman spectrum confirmed the adsorption of plasmids onto the NGWM surface. The D and G bands of the Raman spectra were associated with the disordered sp^2 and sp^2 carbon network of NRGO, respectively (Gómez-Navarro et al., 2007). When NRGO

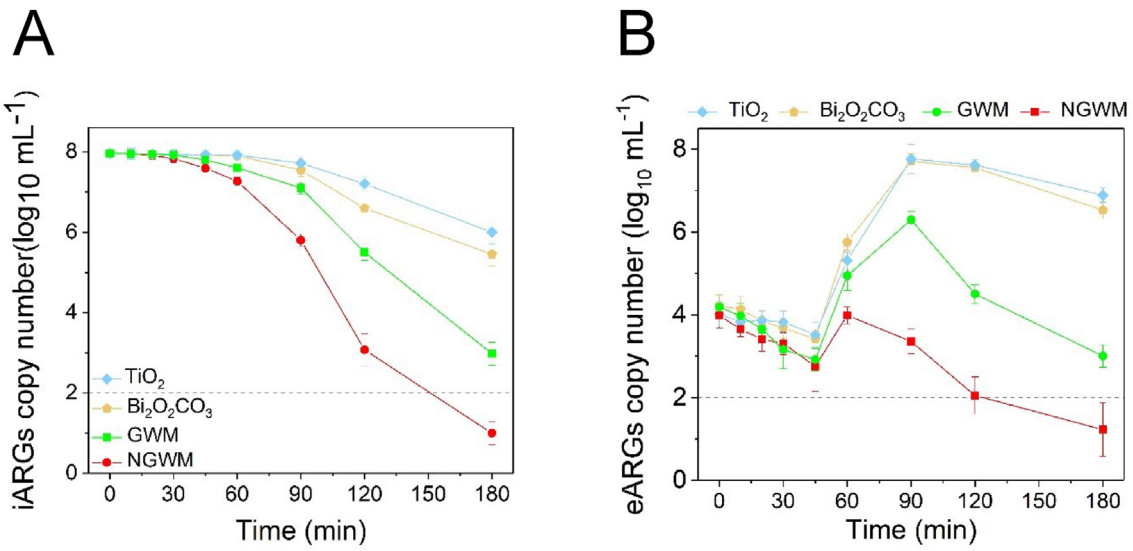

Fig. 5. NRGO wrapping enhanced photocatalytic degradation of bla_{NDM-1} genes from *E. coli* NDM-1 in secondary effluent. NGWM improved intracellular ARG release and degradation (A) and more effectively degraded extracellular ARGs (B) relative to $Bi_2O_2CO_3$ microspheres and TiO_2. Error bars represent ± one standard deviation from the mean of triplicate measurements.

adsorbed plasmid DNA, the NRGO delocalized π-electron and the nucleobase aromatic ring likely disturbed the NRGO π-conjugation through π-π stacking interactions, resulting in sp^2 carbon network disorder/defects and I_D/I_G enhancement thereafter (Yu et al., 2017). Due to the adsorption of plasmids by NGWM, the ratio of D to G band intensity (I_D/I_G) increased by 12.7% (Fig. 6A). Moreover, the I_D/I_G ratio of NGWM rebounded to 0.942 after photocatalytic treatment, indicating that the photogenerated reactive species efficiently degraded the absorbed plasmids.

NGWM-DNA binding was further confirmed by the new stretching vibration of $C{=}N_{nucleobase}$ at 1340 cm^{-1} (Fig. 6B) after plasmid DNA absorption. In return, the hydroxyl groups (HO-C, 1260 cm^{-1}) $_{NRGO}$ and carboxylic groups (HO-C-O, 1039 cm^{-1}) $_{NRGO}$ vibration bands were weakened (Fig. 6B), mainly due to the hydrogen-bond interaction with the amidogen/carbonyl of DNA nucleobase ($HO_{N\text{-}RGO}\text{-}NH_{2nucleobase}$ and $HO_{NRGO}\text{-}O_{nucleobase}$) (Yu et al., 2017). The absorption peaks at 968, 1078, and 1211 cm^{-1} belong to the vibration of the phosphomonoesters dianion (PO_3^{2-}), phosphodiester (PO_2^-) and sugar-phosphate bond (C-O-P), respectively (Movasaghi et al., 2008; Tsuboi, 1957; Yu et al., 2018; Zhao, 2008). These new absorption peaks were observed from NGWM sampled after plasmid absorption, but not from NGWM before treatment (Fig. 6B), implying that the DNA-containing sugar-phosphate backbone was adsorbed on NGWM. Specifically, these new vibration peaks were weakened after photocatalytic treatment, further demonstrating that the adsorbed plasmids could be degraded by photogenerated reactive species.

Photocatalyst stability and reusability. Ensuring photocatalyst stability is critical to practical water treatment and disinfection applications. Hence, we examined the possible photoactivity loss of

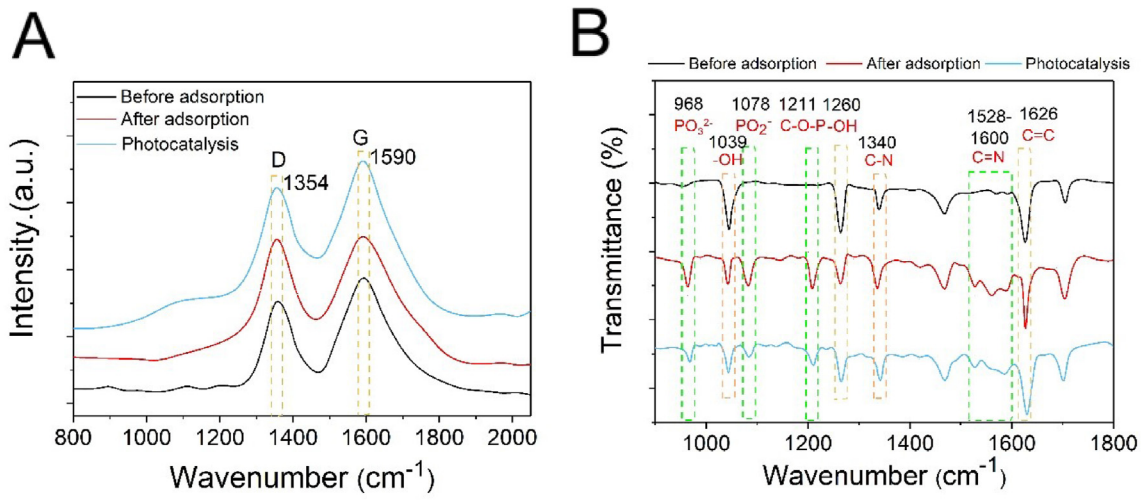

Fig. 6. Interfacial interactions between NGWM and DNA. The Raman spectra (A) and FTIR spectra (B) of NGWM-plasmid complex. The D and G bands of the Raman spectra indicate the disordered sp^3 and sp^2 carbon network of NRGO, respectively. The enhancement of I_D/I_G indicated that plasmid was adsorbed on the NRGO surface through π-π stacking interaction. FTIR shows that the hydroxyl groups (HO-C, 1260 cm^{-1}) $_{NRGO}$ and carboxylic groups (HO-C-O, 1039 cm^{-1}) $_{NRGO}$ vibration bands were weakened, whereas the new absorption peaks at 968, 1078, and 1211 cm^{-1} belong to the vibration of plasmid-containing phosphomonoesters dianion (PO_3^{2-}), phosphodiester (PO_2^-), and the sugar-phosphate bond (C-O-P), respectively, implying that the plasmid was adsorbed on NGWM through the hydrogen-bond interaction, which enhanced its photocatalytic degradation (Fig. 5).

NGWM over consecutive reuse cycles. The photoactivity was relatively stable and no significant decrease in inactivation efficiency was observed after 10 cycles (Fig. S17A). In contrast, the photoactivity of $Bi_2O_2CO_3$ microspheres decreased by 45.7% only after 6 cycles (Fig. S17B). Notably, mass loss and photocorrosion were marginal throughout the test, with about 95.1 ± 0.7% of NGWM recovered after the 10th recycle (Fig. S18). This indicates that NRGO wrapping could efficiently inhibit photocorrosion (i.e., Bi ion leaching) attributed to the effective hybridization of the core photocatalyst with the intimate sheet. Specifically, NRGO could serve as electron acceptors (Tran et al., 2012; Zhao et al., 2018), which likely inhibited further oxidation of NRGO (Fig. S19), and therefore the photoactivity was relatively stable even after ten cycles.

4. Conclusions

Wrapping of hierarchical $Bi_2O_2CO_3$ microspheres with NRGO enhanced bacterial adsorption and photocatalytic ARB inactivation in the secondary effluent (which contains abundant ROS scavengers). Photogenerated electron holes (h^+) and surface-attached hydroxyl radicals ($\bullet OH_{ads}$) were the predominant oxidizing species responsible for ARB inactivation with wrapped microspheres, versus free ROS (e.g., $\bullet OH$, H_2O_2 and $\bullet O_2^-$) for bare microspheres. Due to the short distance between the adsorbed bacteria and photocatalysis reaction sites, eARGs that were released from lysed bacteria were efficiently captured and degraded by the microspheres, thus minimizing ROS scavenging and dilution. The NRGO shell increased the photocatalyst's affinity toward the antibiotic resistant plasmid through π-π stacking and hydrogen-bond interfacial interactions, improving degradation of eARGs. The NRGO shell also served as a protective layer for $Bi_2O_2CO_3$ microspheres, preventing photocorrosion under irradiation, thereby increasing the photocatalyst's lifetime. Overall, this work demonstrates the potential of NRGO wrapping to enhance photocatalytic treatment of secondary effluent and mitigate the dissemination of antibiotic resistance through discharges of secondary effluent from sewage treatment plants.

Declaration of competing interest

The authors declare that they have no known competing financial interests or personal relationships that could have appeared to influence the work reported in this paper.

Acknowledgements

This study was supported by National Natural Science Foundation of China [No. 51625804], the National Key R&D Program of China (2018YFD1100500), NSF ERC on Nanotechnology-Enabled Water Treatment (EEC-1449500), and NSF PIRE grant (OISE-1545756). We thank Huaqiang Chu, Jiabin Chen, Libin Yang, Shaoze Xiao, Danning Zhang and Ling-Li Li for their help on catalyst characterization.

Appendix A. Supplementary data

Supplementary data to this article can be found online at https://doi.org/10.1016/j.watres.2020.116157.

References

Bader, H., Sturzenegger, V., Hoigne, J., 1988. Photometric method for the determination of low concentrations of hydrogen peroxide by the peroxidase catalyzed oxidation of N, N-diethyl-p-phenylenediamine (DPD). Water Res. 22 (9), 1109–1115.

Cho, M., Chung, H., Choi, W., Yoon, J., 2004. Linear correlation between inactivation of E. coli and OH radical concentration in TiO_2 photocatalytic disinfection. Water Res. 38 (4), 1069–1077.

Davies, J., Davies, D., 2010. Origins and evolution of antibiotic resistance. Microbiol. Mol. Biol. Rev. 74 (3), 417–433.

Dong, F., Ho, W.-K., Lee, S., Wu, Z., Fu, M., Zou, S., Huang, Y., 2011. Template-free fabrication and growth mechanism of uniform $(BiO)_2CO_3$ hierarchical hollow microspheres with outstanding photocatalytic activities under both UV and visible light irradiation. J. Mater. Chem. 21 (33), 12428–12436.

Dotson, A.D., Metz, D., Linden, K.G., 2010. UV/H2O2 treatment of drinking water increases post-chlorination DBP formation. Water Res. 44 (12), 3703–3713.

Dunlop, P., Ciavola, M., Rizzo, L., McDowell, D., Byrne, J., 2015. Effect of photocatalysis on the transfer of antibiotic resistance genes in urban wastewater. Catal. Today 240, 55–60.

Gómez-Navarro, C., Weitz, R.T., Bittner, A.M., Scolari, M., Mews, A., Burghard, M., Kern, K., 2007. Electronic transport properties of individual chemically reduced graphene oxide sheets. Nano Lett. 7 (11), 3499–3503.

Geeraerd, A., Valdramidis, V., Van Impe, J., 2005. GInaFiT, a freeware tool to assess non-log-linear microbial survivor curves. Int. J. Food Microbiol. 102 (1), 95–105.

Giandomenico, A.R., Cerniglia, G.E., Biaglow, J.E., Stevens, C.W., Koch, C.J., 1997. The importance of sodium pyruvate in assessing damage produced by hydrogen peroxide. Free Radic. Biol. Med. 23 (3), 426–434.

Giannakis, S., Le, T.-T.M., Entenza, J.M., Pulgarin, C., 2018. Solar photo-Fenton disinfection of 11 antibiotic-resistant bacteria (ARB) and elimination of representative AR genes. Evidence that antibiotic resistance does not imply resistance to oxidative treatment. Water Res. 143, 334–345.

Gogniat, G., Dukan, S., 2007. TiO_2 photocatalysis causes DNA damage via fenton reaction-generated hydroxyl radicals during the recovery period. Appl. Environ. Microbiol. 73 (23), 7740–7743.

Hasan, S.A., Tsekoura, E.K., Sternhagen, V., Strømme, M., 2012. Evolution of the composition and suspension performance of nitrogen-doped graphene. J. Phys. Chem. C 116 (11), 6530–6536.

He, H., Zhou, P., Shimabuku, K.K., Fang, X., Li, S., Lee, Y., Dodd, M.C., 2019. Degradation and deactivation of bacterial antibiotic resistance genes during exposure to free chlorine, monochloramine, chlorine dioxide, ozone, ultraviolet light, and hydroxyl radical. Environ. Sci. Technol. 53 (4), 2013–2026.

Hu, X., Zhou, Q., 2013. Health and ecosystem risks of graphene. Chem. Rev. 113 (5), 3815–3835.

Jiang, Q., Yin, H., Li, G., Liu, H., An, T., Wong, P.K., Zhao, H., 2017. Elimination of antibiotic-resistance bacterium and its associated/dissociative blaTEM-1 and aac (3)-II antibiotic-resistance genes in aqueous system via photo-electrocatalytic process. Water Res. 125, 219–226.

Ju, F., Li, B., Ma, L., Wang, Y., Huang, D., Zhang, T., 2016. Antibiotic resistance genes and human bacterial pathogens: co-occurrence, removal, and enrichment in municipal sewage sludge digesters. Water Res. 91, 1–10.

Karaolia, P., Michael-Kordatou, I., Hapeshi, E., Drosou, C., Bertakis, Y., Christofilos, D., Armatas, G.S., Sygellou, L., Schwartz, T., Xekoukoulotakis, N.P., 2018. Removal of antibiotics, antibiotic-resistant bacteria and their associated genes by graphene-based TiO_2 composite photocatalysts under solar radiation in urban wastewaters. Appl. Catal. B Environ. 224, 810–824.

Koenig, S.P., Boddeti, N.G., Dunn, M.L., Bunch, J.S., 2011. Ultrastrong adhesion of graphene membranes. Nat. Nanotechnol. 6 (9), 543.

Li, D., Zeng, S., He, M., Gu, A.Z., 2016. Water disinfection byproducts induce antibiotic resistance-role of environmental pollutants in resistance phenomena. Environ. Sci. Technol. 50 (6), 3193–3201.

Li, L.-L., Yu, P., Wang, X., Yu, S.-S., Mathieu, J., Yu, H.-Q., Alvarez, P.J.J., 2017. Enhanced biofilm penetration for microbial control by polyvalent phages conjugated with magnetic colloidal nanoparticle clusters (CNCs). Environ. Sci.: Nano 4 (9), 1817–1826.

Liang, J., Liu, F., Deng, J., Li, M., Tong, M., 2017. Efficient bacterial inactivation with Z-scheme AgI/Bi_2MoO_6 under visible light irradiation. Water Res. 123, 632–641.

Liang, Y.T., Vijayan, B.K., Gray, K.A., Hersam, M.C., 2011. Minimizing graphene defects enhances titania nanocomposite-based photocatalytic reduction of CO_2 for improved solar fuel production. Nano Lett. 11 (7), 2865–2870.

Lorenz, M.G., Wackernagel, W., 1994. Bacterial gene transfer by natural genetic transformation in the environment. Microbiol. Mol. Biol. Rev. 58 (3), 563–602.

Luo, Y., Xu, L., Rysz, M., Wang, Y., Zhang, H., Alvarez, P.J., 2011. Occurrence and transport of tetracycline, sulfonamide, quinolone, and macrolide antibiotics in the Haihe River Basin, China. Environ. Sci. Technol. 45 (5), 1827–1833.

Luo, Y., Yang, F., Mathieu, J., Mao, D., Wang, Q., Alvarez, P.J.J., 2014. Proliferation of multidrug-resistant New Delhi metallo-β-lactamase genes in municipal wastewater treatment plants in Northern China. Environ. Sci. Technol. Lett. 1 (1), 26–30.

Ma, S., Zhan, S., Jia, Y., Shi, Q., Zhou, Q., 2016. Enhanced disinfection application of Ag-modified g-C_3N_4 composite under visible light. Appl. Catal. B Environ. 186, 77–87.

Meyer, J.C., Geim, A.K., Katsnelson, M.I., Novoselov, K.S., Booth, T.J., Roth, S., 2007. The structure of suspended graphene sheets. Nature 446 (7131), 60–63.

Moreira, N.F., Narciso-da-Rocha, C., Polo-López, M.I., Pastrana-Martínez, L.M., Faria, J.L., Manaia, C.M., Fernández-Ibáñez, P., Nunes, O.C., Silva, A.M., 2018. Solar treatment (H_2O_2, TiO_2-P25 and GO-TiO_2 photocatalysis, photo-Fenton) of organic micropollutants, human pathogen indicators, antibiotic resistant bacteria and related genes in urban wastewater. Water Res. 135, 195–206.

Mou, Z., Wu, Y., Sun, J., Yang, P., Du, Y., Lu, C., 2014. TiO_2 nanoparticles-functionalized N-doped graphene with superior interfacial contact and enhanced charge separation for photocatalytic hydrogen generation. ACS Appl.

Mater. Interfaces 6 (16), 13798–13806.
Movasaghi, Z., Rehman, S., ur Rehman, D.I., 2008. Fourier transform infrared (FTIR) spectroscopy of biological tissues. Appl. Spectrosc. Rev. 43 (2), 134–179.
Ng, T.W., Zhang, L., Liu, J., Huang, G., Wang, W., Wong, P.K., 2016. Visible-light-driven photocatalytic inactivation of Escherichia coli by magnetic Fe_2O_3–AgBr. Water Res. 90, 111–118.
O'Neill, J., 2016. Review on Antimicrobial Resistance: Tackling a Crisis for the Health and Wealth of Nations. HM Government, London, 2014.
Pelaez, M., Nolan, N.T., Pillai, S.C., Seery, M.K., Falaras, P., Kontos, A.G., Dunlop, P.S., Hamilton, J.W., Byrne, J.A., O'shea, K., Entezari, M.H., Dionysiou, D.D., 2012. A review on the visible light active titanium dioxide photocatalysts for environmental applications. Appl. Catal. B Environ. 125, 331–349.
Ren, S., Boo, C., Guo, N., Wang, S., Elimelech, M., Wang, Y., 2018. Photocatalytic reactive ultrafiltration membrane for removal of antibiotic resistant bacteria and antibiotic resistance genes from wastewater effluent. Environ. Sci. Technol. 52 (15), 8666–8673.
Ribeiro, A.R.L., Moreira, N.F., Puma, G.L., Silva, A.M., 2019. Impact of water matrix on the removal of micropollutants by advanced oxidation technologies. Chem. Eng. J. 363, 155–173.
Rinta-Kanto, J.M., Lehtola, M.J., Vartiainen, T., Martikainen, P.J., 2004. Rapid enumeration of virus-like particles in drinking water samples using SYBR green I-staining. Water Res. 38 (10), 2614–2618.
Smith, D.E., Dhinojwala, A., Moore, F.B.-G., 2019. Effect of substrate and bacterial zeta potential on adhesion of Mycobacterium smegmatis. Langmuir 35 (21), 7035–7042.
Spasiano, D., Marotta, R., Malato, S., Fernandez-Ibanez, P., Di Somma, I., 2015. Solar photocatalysis: materials, reactors, some commercial, and pre-industrialized applications. A comprehensive approach. Appl. Catal. B Environ. 170, 90–123.
Sun, H., Li, G., Nie, X., Shi, H., Wong, P.-K., Zhao, H., An, T., 2014. Systematic approach to in-depth understanding of photoelectrocatalytic bacterial inactivation mechanisms by tracking the decomposed building blocks. Environ. Sci. Technol. 48 (16), 9412–9419.
Teng, Z., Yang, N., Lv, H., Wang, S., Hu, M., Wang, C., Wang, D., Wang, G., 2019. Edge-functionalized g-C3N4 nanosheets as a highly efficient metal-free photocatalyst for safe drinking water. Inside Chem. 5 (3), 664–680.
Tran, P.D., Batabyal, S.K., Pramana, S.S., Barber, J., Wong, L.H., Loo, S.C.J., 2012. A cuprous oxide–reduced graphene oxide (Cu_2O–rGO) composite photocatalyst for hydrogen generation: employing rGO as an electron acceptor to enhance the photocatalytic activity and stability of Cu_2O. Nanoscale 4 (13), 3875–3878.
Tsuboi, M., 1957. Vibrational spectra of phosphite and hypophosphite anions, and the characteristic frequencies of PO_3^- and PO_2^- groups. J. Am. Chem. Soc. 79 (6), 1351–1354.
Vesper, S.J., 1987. Production of pili (fimbriae) by Pseudomonas fluorescens and correlation with attachment to corn roots. Appl. Environ. Microbiol. 53 (7), 1397–1405.
Wang, W., Yu, Y., An, T., Li, G., Yip, H.Y., Yu, J.C., Wong, P.K., 2012. Visible-light-driven photocatalytic inactivation of E. coli K-12 by bismuth vanadate nanotubes: bactericidal performance and mechanism. Environ. Sci. Technol. 46 (8), 4599–4606.
Xia, D., An, T., Li, G., Wang, W., Zhao, H., Wong, P.K., 2016. Synergistic photocatalytic inactivation mechanisms of bacteria by graphene sheets grafted plasmonic AgAgX (X= Cl, Br, I) composite photocatalyst under visible light irradiation. Water Res. 99, 149–161.
Xia, D., Ng, T.W., An, T., Li, G., Li, Y., Yip, H.Y., Zhao, H., Lu, A., Wong, P.-K., 2013. A recyclable mineral catalyst for visible-light-driven photocatalytic inactivation of bacteria: natural magnetic sphalerite. Environ. Sci. Technol. 47 (19), 11166–11173.
Xia, D., Shen, Z., Huang, G., Wang, W., Yu, J.C., Wong, P.K., 2015. Red phosphorus: an earth-abundant elemental photocatalyst for "green" bacterial inactivation under visible light. Environ. Sci. Technol. 49 (10), 6264–6273.
Xu, Y., Mo, Y., Tian, J., Wang, P., Yu, H., Yu, J., 2016. The synergistic effect of graphitic N and pyrrolic N for the enhanced photocatalytic performance of nitrogen-doped graphene/TiO_2 nanocomposites. Appl. Catal. B Environ. 181, 810–817.
Xue, J., BinAhmed, S., Wang, Z., Karp, N.G., Stottrup, B.L., Romero-Vargas Castrillón, S., 2018. Bacterial adhesion to graphene oxide (GO)-functionalized interfaces is determined by hydrophobicity and GO sheet spatial orientation. Environ. Sci. Technol. Lett. 5 (1), 14–19.
Yu, M., Niu, Y., Zhang, J., Zhang, H., Yang, Y., Taran, E., Jambhrunkar, S., Gu, W., Thorn, P., Yu, C., 2016. Size-dependent gene delivery of amine-modified silica nanoparticles. Nano Res. 9 (2), 291–305.
Yu, W., Zhan, S., Shen, Z., Zhou, Q., 2018. A newly synthesized Au/GO-Co_3O_4 composite effectively inhibits the replication of tetracycline resistance gene in water. Chem. Eng. J. 345, 462–470.
Yu, W., Zhan, S., Shen, Z., Zhou, Q., Yang, D., 2017. Efficient removal mechanism for antibiotic resistance genes from aquatic environments by graphene oxide nanosheet. Chem. Eng. J. 313, 836–846.
Zhang, D., Lee, C., Javed, H., Yu, P., Kim, J.-H., Alvarez, P.J., 2018. Easily recoverable, micrometer-sized TiO_2 hierarchical spheres decorated with cyclodextrin for enhanced photocatalytic degradation of organic micropollutants. Environ. Sci. Technol. 52 (21), 12402–12411.
Zhang, H., Lv, X., Li, Y., Wang, Y., Li, J., 2010a. P25-graphene composite as a high performance photocatalyst. ACS Nano 4 (1), 380–386.
Zhang, L.-S., Wong, K.-H., Yip, H.-Y., Hu, C., Yu, J.C., Chan, C.-Y., Wong, P.-K., 2010b. Effective photocatalytic disinfection of E. coli K-12 using AgBr–Ag–Bi_2WO_6 nanojunction system irradiated by visible light: the role of diffusing hydroxyl radicals. Environ. Sci. Technol. 44 (4), 1392–1398.
Zhang, W., Li, Y., Wang, C., Wang, P., Wang, Q., 2013. Energy recovery during advanced wastewater treatment: simultaneous estrogenic activity removal and hydrogen production through solar photocatalysis. Water Res. 47 (3), 1480–1490.
Zhang, Y., Gu, A.Z., He, M., Li, D., Chen, J., 2017. Subinhibitory concentrations of disinfectants promote the horizontal transfer of multidrug resistance genes within and across genera. Environ. Sci. Technol. 51 (1), 570–580.
Zhang, Y., Li, D., Zhang, Y., Zhou, X., Guo, S., Yang, L., 2014. Graphene-wrapped $Bi_2O_2CO_3$ core–shell structures with enhanced quantum efficiency profit from an ultrafast electron transfer process. J. Mater. Chem. 2 (22), 8273–8280.
Zhao, H., Yu, H., Quan, X., Chen, S., Zhang, Y., Zhao, H., Wang, H., 2014a. Fabrication of atomic single layer graphitic-C3N4 and its high performance of photocatalytic disinfection under visible light irradiation. Appl. Catal. B Environ. 152, 46–50.
Zhao, H., Zhang, C., Wang, Y., Chen, W., Alvarez, P.J., 2018. Self-damaging aerobic reduction of graphene oxide by escherichia coli: role of GO-mediated extracellular superoxide formation. Environ. Sci. Technol. 52 (21), 12783–12791.
Zhao, W., Walker, S.L., Huang, Q., Cai, P., 2014b. Adhesion of bacterial pathogens to soil colloidal particles: influences of cell type, natural organic matter, and solution chemistry. Water Res. 53, 35–46.
Zhao, X., 2008. Interaction of C60 derivatives and ssDNA from simulations. J. Phys. Chem. C 112 (24), 8898–8906.
Zhou, D., Xu, Z., Dong, S., Huo, M., Dong, S., Tian, X., Cui, B., Xiong, H., Li, T., Ma, D., 2015. Intimate coupling of photocatalysis and biodegradation for degrading phenol using different light types: visible light vs UV light. Environ. Sci. Technol. 49 (13), 7776–7783.